

# Localization and interaction of interlayer excitons in MoSe<sub>2</sub>/WSe<sub>2</sub> heterobilayers

Hanlin Fang,<sup>1,\*</sup> Qiaoling Lin,<sup>2</sup> Yi Zhang,<sup>3</sup> Joshua Thompson,<sup>4</sup> Sanshui Xiao,<sup>2</sup> Zhipei Sun,<sup>3</sup> Ermin Malic,<sup>4</sup> Saroj Dash,<sup>1</sup> and Witlef Wieczorek<sup>1,†</sup>

<sup>1</sup>*Department of Microtechnology and Nanoscience (MC2),  
Chalmers University of Technology, SE-412 96 Göteborg, Sweden*

<sup>2</sup>*Department of Electrical and Photonics Engineering,  
Technical University of Denmark, DK-2800, Kongens Lyngby Denmark*

<sup>3</sup>*Department of Electronics and Nanoengineering and QTF Centre of Excellence, Aalto University, 02150 Espoo, Finland*

<sup>4</sup>*Department of Physics, Philipps-Universität Marburg, 35037 Marburg, Germany*

(Dated: July 11, 2023)

Transition metal dichalcogenide (TMD) heterobilayers provide a versatile platform to explore unique excitonic physics via properties of the constituent TMDs and external stimuli. Interlayer excitons (IXs) can form in TMD heterobilayers as delocalized or localized states. However, the localization of IX in different types of potential traps, the emergence of biexcitons in the high-excitation regime, and the impact of potential traps on biexciton formation have remained elusive. In our work, we observe two types of potential traps in a MoSe<sub>2</sub>/WSe<sub>2</sub> heterobilayer, which result in significantly different emission behavior of IXs at different temperatures. We identify the origin of these traps as localized defect states and the moiré potential of the TMD heterobilayer. Furthermore, with strong excitation intensity, a superlinear emission behavior indicates the emergence of interlayer biexcitons, whose formation peaks at a specific temperature. Our work elucidates the different excitation and temperature regimes required for the formation of both localized and delocalized IX and biexcitons, and, thus, contributes to a better understanding and application of the rich exciton physics in TMD heterostructures.

Transition metal dichalcogenide (TMD) heterostructures provide a versatile 2D material platform to explore unique excitonic phenomena [1, 2] including the realization of hybridized excitons [3], excitonic Mott insulators [4], and excitonic Bose-Einstein condensation [5]. TMD heterobilayers with type-II band alignment can host interlayer excitons (IXs), which consist of an electron and a hole that after a fast charge transfer process are located in the different constituent TMD monolayers [6, 7]. The dipolar exciton nature provides the IX states with a long exciton lifetime [8], high valley polarization degree [9], and high electric field tunability [10], paving the way to excitonic optoelectronic applications [11]. The properties of IXs are strongly affected by the twist angle of the heterostructure [12, 13], which modulates the energy landscape in the material and forms a moiré potential. Stacked TMD monolayers with small twist angles (typically less than 2° or larger than 58°) result in a strong moiré effect, which is manifested by characteristic emission features of moiré-trapped IXs [14–16]. Such IXs could serve as quantum emitter arrays [12], realize optical nonlinearities [17], and explore many-body physics [18]. Experimentally, the localization of excitons in the moiré potential has been demonstrated by time-resolved and angle-resolved photoemission spectroscopy [19, 20], exciton transport measurements [21], and electron-beam-based hyperspectral imaging [22].

An exemplary TMD heterobilayer system is MoSe<sub>2</sub>/WSe<sub>2</sub>, where two types of features are as-

cribed to moiré excitons that have been observed in the photoluminescence (PL) spectrum [14, 23–25]. The first feature is sharp emission lines with a linewidth of  $\sim 100 \mu\text{eV}$ , which show not a systematic change with twist angle [23]. The second feature is characterized by multi-peaked emission features, where the individual peaks have a linewidth on the order of 20 meV and their energy spacing depends on the twist angle, which is in agreement with a quantum harmonic oscillator model of the moiré potential [14]. Notably, the moiré potential can enhance the interaction between excitons and in that way enables the formation of many-body excitonic states, such as biexcitons [26]. However, the transition and relation between these excitonic features as well as the emergence of interlayer biexcitons (IXXs) in the strong excitation regime have not been explored so far.

In our work, we observe the two typical IX emission features mentioned above in the same H-stacked MoSe<sub>2</sub>/WSe<sub>2</sub> heterobilayer. We find that these two types of IXs dominate the PL emission spectrum at different temperature ranges, thereby extending previous studies [14, 23]. We show that the two emission features can be explained by the presence of two types of potential traps, of which one is shallow ( $\sim 4 \text{ meV}$ ) and possibly related to defect potentials, and the other one is deep ( $\sim 27 \text{ meV}$ ) and attributed to the moiré potential. At large excitation intensity, the dipolar interaction between the IXs enables the observation of the signature of PL emission originating from IXXs. We find that the conversion between IX and IXX reaches a maximal value at a temperature of 30 K, which correlates with the temperature at which the IX emission associated with the shallow potential traps is quenched.

\* [hanlin.fang@chalmers.se](mailto:hanlin.fang@chalmers.se)

† [witlef.wieczorek@chalmers.se](mailto:witlef.wieczorek@chalmers.se)

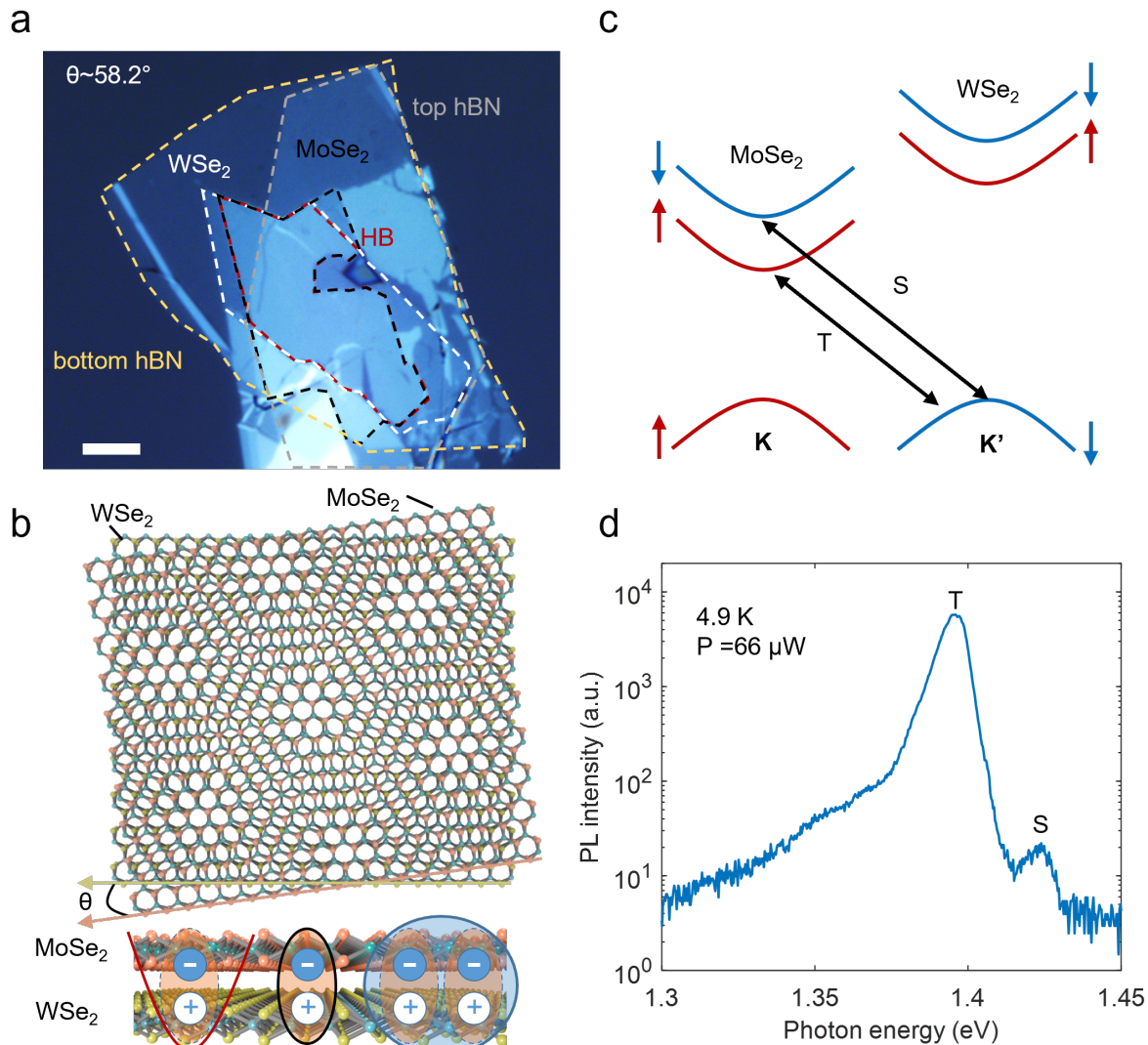


FIG. 1. Interlayer excitons in an hBN encapsulated H-stacked MoSe<sub>2</sub>/WSe<sub>2</sub> heterobilayer sample. (a) Bright-field optical image of the heterostructure on a fused silica substrate. HB (dashed red) is the MoSe<sub>2</sub>/WSe<sub>2</sub> heterobilayer with a twist angle of  $\theta \sim 58.2^\circ$ . Scale bar: 5  $\mu\text{m}$ . (b) Schematic of a twisted heterobilayer exhibiting a moiré pattern. It can host different excitonic states, such as localized IXs (red), delocalized IXs (black), and biexcitons (blue). (c) Band diagram of the heterobilayer showing the two typical exciton transitions: spin-singlet IX (S) and spin-triplet IX (T). (d) Semilog plot of the PL spectrum of the heterobilayer at 4.9K in the intermediate excitation regime with the S and T emissions marked.

### I. INTERLAYER EXCITONS IN A TMD HETEROBILAYER

Fig. 1a shows an optical microscope image of our 2D heterostructure fabricated via the van der Waals pickup method (details in Methods). The MoSe<sub>2</sub>/WSe<sub>2</sub> heterobilayer is encapsulated by thin-hBN flakes to reduce the inhomogeneous screening from the substrate [27], enabling the observation of multiple moiré-related excitonic resonances [14]. The constituent monolayers are twisted with an angle of  $\sim 58.2^\circ$  (see Fig. S1), thus, forming a moiré superlattice that can host various exciton states (see Fig. 1b). Note that atomic reconstruction

[28] would impact the moiré superlattice for small twist angles (about  $\leq 1^\circ$  or  $\geq 59^\circ$  in a MoSe<sub>2</sub>/WSe<sub>2</sub> heterobilayer), which we expect not to be the case in our sample. The spin-orbit coupling (SOC) results in a sizeable energy level splitting of the conduction band of MoSe<sub>2</sub>, permitting the formation of spin-conserved singlet (S) and spin-forbidden triplet (T) IX states as shown in Fig. 1c. Unlike TMD monolayers that host optically dark spin-flip excitons, the heterobilayer structure breaks the mirror symmetry of the material and brightens the T-IXs [29].

We first pump the heterobilayer in an intermediate excitation regime (pump power of 66  $\mu\text{W}$ ) by a continuous wave (cw)  $\sim 730$  nm (corresponding to  $\sim 1.7$  eV) laser

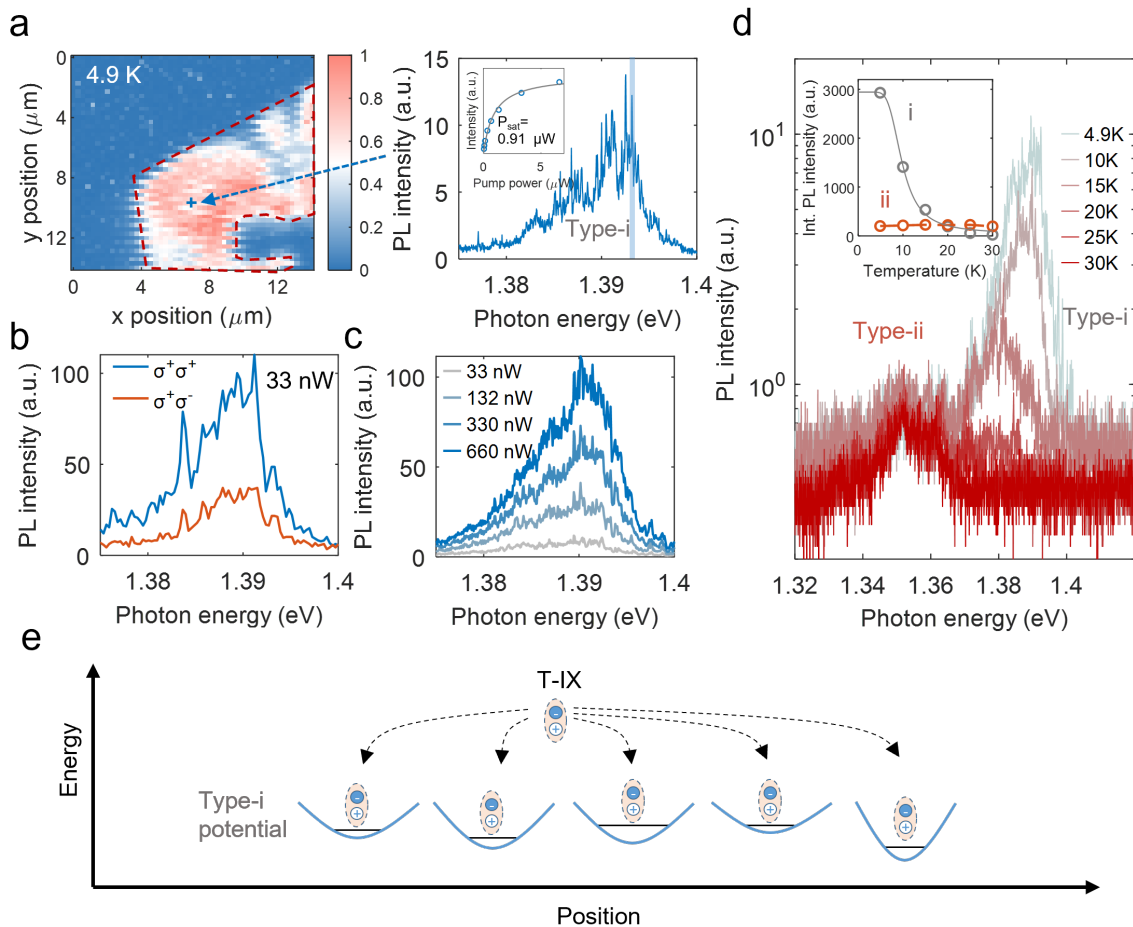


FIG. 2. Localized IXs (type-i IXs) in the weak excitation regime. (a) PL map with a pump power of 33 nW and at 4.9 K. The right panel shows the PL spectrum of sharp emission lines (denoted as type-i emission). The integrated PL intensity of a sharp emission line with pump power is fitted with the formula:  $I = I_{\max}/(1 + P_{\text{sat}}/P)$ , where  $P_{\text{sat}} \sim 0.91 \mu\text{W}$  is the saturation power. (b) Valley polarization measurement of the type-i emission. (c) Power-dependent PL spectrum. (d) PL spectrum in dependence on temperature with a pump power of 33 nW revealing two types of localized IXs. The inset shows the temperature-dependent PL intensity of two localized IX, where the integrated PL intensity of type-i IXs is fitted by an Arrhenius equation. (e) Physical picture of type-i potential traps that confine the T-IXs. A potential depth of  $\sim 4 \text{ meV}$  is derived from the thermal activation energy.

near-resonant to the intralayer exciton of  $\text{WSe}_2$ . Two interlayer excitonic states (peak at  $\sim 1.4 \text{ eV}$  and  $\sim 1.425 \text{ eV}$ , labeled as T and S, respectively) are observed in the PL emission of the heterobilayer (Fig. 1d). The two peaks are further characterized by polarization-dependent PL measurements, whereby the S-IX shows the expected cross-polarized and the T-IX co-polarized emission with the pump (see Fig. S2). The observed energy splitting of  $\sim 25 \text{ meV}$  together with the measured valley polarization of the two peaks are in agreement with previous measurements of the SOC-induced singlet and triplet interlayer excitons [9, 30].

## II. TRAPPED INTERLAYER EXCITONS

We now turn to the PL characteristics of the heterobilayer in the weak excitation regime for investigating the localization of IXs. To this end, we use a pump power of 33 nW and record a PL map of the sample at 4.9 K (Fig. 2a). We observe sharp emission lines with linewidths of  $\sim 100 \mu\text{eV}$  in the PL spectrum (right panel of Fig. 2a), which is consistent with previous work [23] (see Fig. S3 for additional spectra). We denote this emission feature as type-i and the related IXs as type-i IXs. The type-i IXs show a clear saturation behavior with a low saturation power of  $\sim 0.91 \mu\text{W}$  (inset of Fig. 2a), which is similar to previously reported single-photon emitters in  $\text{MoSe}_2/\text{WSe}_2$  heterobilayers [24]. The observed type-i IXs show co-polarized PL emission with

the circularly polarized pump (see Fig. 2b), manifesting that the trapped IXs are of T-type [9, 30]. Further, with increased temperature, we observe that the PL intensity of the type-i IXs decreases (Fig. 2d). By fitting the temperature-dependent PL intensity with an Arrhenius law, we extract a thermal activation energy of  $\sim 4$  meV (see Supplementary Note 1), which yields the depth of the type-i potential trap [26]. The type-i IX red-shifts upon temperature increase, which is due to the relatively fast PL quenching of the higher energy states requiring less energy for delocalization.

The widespread spatial distribution and emission energies of type-i IXs (see Fig. S3) are in principle consistent with previous works [21, 23, 24, 31] that relate it to moiré-trapped IXs. In that case, two physical models have been proposed: (a) the occupation of IXs in many quantized energy levels with small energy spacing defined by the moiré potential [21, 31], or (b) the occupation of IXs in single quantized energy levels, whereby the broad spectral emission range is ascribed to moiré IXs trapped within moiré potential traps, which are different due to fabrication-related distortions [23]. Model (a) would predict an increased occupation possibility of IXs in high energy levels with increasing excitation. However, this exciton-filling feature has not been observed in previous works [21, 31]. In our measurements, we find that with increasing pump power (Fig. 2c), the sharp emission lines emerge into broad peaks, and no clear relative intensity change between the emission peaks is observed. Hence, this overall behavior excludes model (a) and would point toward model (b), which is similar to recent works [25, 32].

We will come back to the origin of the type-i emission feature, but will first discuss the spectral feature that we observe at higher temperatures (Fig. 2d), where we find that another peak with lower energy (denoted as type-ii) dominates the PL spectrum (Fig. S4). This temperature-dependent behavior can be explained by the presence of deeper potential traps that host type-ii IXs. To further explore the nature of the type-ii IXs, the sample temperature is raised to about 40 K to suppress type-i IXs. Then, the PL emission of type-ii IXs features multiple broad emission peaks in the intermediate excitation regime (at an excitation power of  $13.2 \mu\text{W}$ , see Fig. 3a), similar PL spectra measured at other positions on the heterobilayer are shown in Fig. S5. Fig. 3a shows the evolution of these multiple peaks with pump power. We find that the lowest energy state at  $\sim 1.342$  eV dominates the PL spectrum at the lowest pump power, while the PL intensity of higher-energy states lying between 1.352 eV and 1.37 eV grows faster than that of the lower-energy states with increasing pump power. By integrating the PL intensity of those peaks, we extract a clear sublinear power law behavior (Fig. 3b), which indicates that the lower energy states saturate faster than higher energy states. Note that the delocalized T-IX shows instead a linear, power-dependent behavior. This exciton-filling feature reflects the presence of quantized energy levels originating from the moiré po-

tential, in agreement with previous works about moiré IXs [8, 14, 33]. To estimate the depth of the moiré potential traps, we record the integrated PL intensity of type-ii IXs as a function of temperature and fit it with an Arrhenius equation, which yields a value of  $\sim 27$  meV (see Fig. S6). This moiré potential of finite depth will result in a decreasing energy spacing between quantized levels within the potential and, eventually, converge into a continuum, which is illustrated in Fig. 3c. The multiple peaks (with energy below 1.38 eV) originate from the radiative recombination of IX occupied in different energy levels. The absence of clear emission features between 1.37 eV and 1.4 eV can be understood by the small energy spacing of the adjacent levels in the moiré potential. Hence, we identify type-ii IXs as moiré IXs.

Let us now come back to examine more closely the nature of type-i IX. To this end, we also measured the exciton lifetime [14, 23] of type-i and type-ii IXs (see Fig. S7). Compared to type-i IXs with a slow decay of  $\sim 235$  ns, the type-ii IXs show a lifetime that is one order of magnitude shorter ( $\sim 23$  ns, see Fig. S7). This large difference in lifetime indicates that the two types of localized IXs originate from spatially different potential traps, which is consistent with observing the two types of emission behavior in Fig. 2(d), instead of a single emission feature only [34]. Theoretically, it was shown that two types of moiré-related potential traps can exist at different high symmetry registries, i.e.,  $H_h^h$  and  $H_h^X$ , having different potential depths [12]. It is predicted that the emission related to these two types of traps should show opposite circular polarization behavior [12]. However, we find that the emission of both type-i and type-ii IXs is co-polarized with a circularly-polarized pump (see Fig. 2b and Fig. S8). Thus, type-i IXs in our sample cannot originate from the moiré potential. As mentioned above, the emission of type-i IXs is nearly suppressed at 30 K (see Fig. 2d and Fig. S4), which is consistent with already reported defect-bound single excitons [35, 36]. Additionally, even high quality flux-grown crystals that we use for fabricating our TMD heterobilayer are expected to have at least  $10^3$  point defects per  $1 \mu\text{m}^2$  [37]. Hence, we conclude that the type-i emission feature is related to defect-bound IX.

### III. INTERLAYER BIEXCITONS

To explore the formation of many-body excitonic states with the presence of potential traps in the TMD heterobilayer, we studied the PL emission at even higher pump powers, but remaining at a low temperature of 4.9 K (see Fig. 4a). We observe three prominent resonances: peak T at  $\sim 1.399$  eV and peak S (both as in Fig. 1d) and peak Z at  $\sim 1.424$  eV, where peak T(S) is assigned to the T(S)-IX. By examining the PL intensity of the three peaks, we find that the intensity of peak Z grows faster with increasing pump power (Fig. 4a). To quantify that, we fit the integrated intensity of the three peaks with the usual



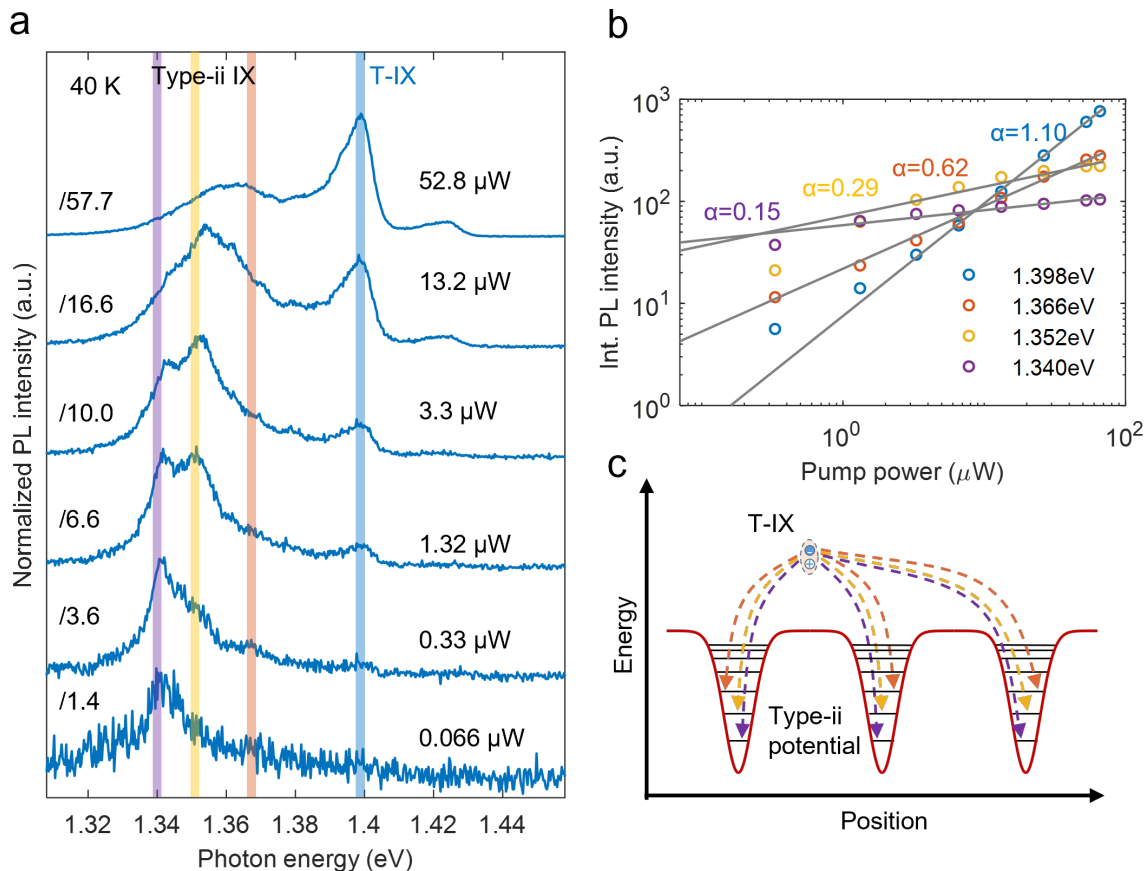


FIG. 3. Formation of type-ii IXs and their filling into moiré potential traps. (a) PL spectrum as a function of pump power at an elevated temperature of 40 K. The PL emission of T-IXs ( $\sim 1.4$  eV) dominates the spectrum with an increase in pump power. Each spectrum is normalized with its own peak intensity. (b) Logarithmic plot of the integrated PL intensity (with an energy range of  $\sim 3$  meV) of different IX states marked in (a). The data are fitted by a power-law relation of the form  $P^\alpha$ . (c) Physical picture of the moiré potential traps that confine IXs in quantized energy levels.

power law  $\propto P^\alpha$ . The fits yield  $\alpha \sim 1.41$  for the Z peak, while  $\alpha \sim 0.54$  for the T peak, and  $\alpha \sim 1.04$  for the S peak. The superlinear behavior of the Z peak is a typical feature of PL emission related to biexcitons. Ideally,  $\alpha$  should be 2, but values between 1.2 to 1.9 have been typically observed for emission related to biexcitons in monolayer TMDs [38] or quantum wells [39]. We exclude other mechanisms explaining the superlinear behavior such as superradiance [40] or Bose-Einstein condensation [5], as both would come with linewidth narrowing, which we do not observe. Thus, we attribute the observed Z feature to the emission of biexcitons. Note that the measured IXX emission energy is the same as for the S-IX, which means a zero binding energy if the IXX originates from the interaction of S-IXs. Alternatively, the formation of IXXs can come from interacting T-IXs. As peak Z has a  $\sim 25$  meV higher energy than the T peak, the underlying exciton-exciton interaction leading to the formation of biexcitons would then be repulsive [26, 41, 42].

To study the formation of IXXs in our sample, we measured their PL emission in dependence of temperature.

Fig. 4c shows that the exponent  $\alpha$  of peak Z reaches a maximum value of  $\sim 1.8$  at about 30 K. Interestingly, the exponent of peak T increases to a value of about 1 at the same temperature of 30 K (consistent with our measurements presented in Fig. 3), and remains at this value at higher temperatures. This threshold behavior at a temperature of 30 K observed for the Z and the T peak matches remarkably well with the temperature that quenches type-i IXs. Hence, we hypothesize that the type-i potential traps have an influence on the formation of IXXs and the T-IX. This temperature-dependent change of  $\alpha$  can be reproduced in another sample with a smaller twist angle (Fig. S9). In contrast, the moiré potential is almost unaffected at that temperature and fully filled in the strong excitation regime, permitting one to rule out its influence on the generation of IXXs.

We suggest the following physical picture (see Fig. 4d) to explain the influence of the two types of potential traps on the formation of IXXs at a low temperature of 4.9 K. With increasing pump power, the lower energy levels of the moiré potential with larger energy spacing get gradu-

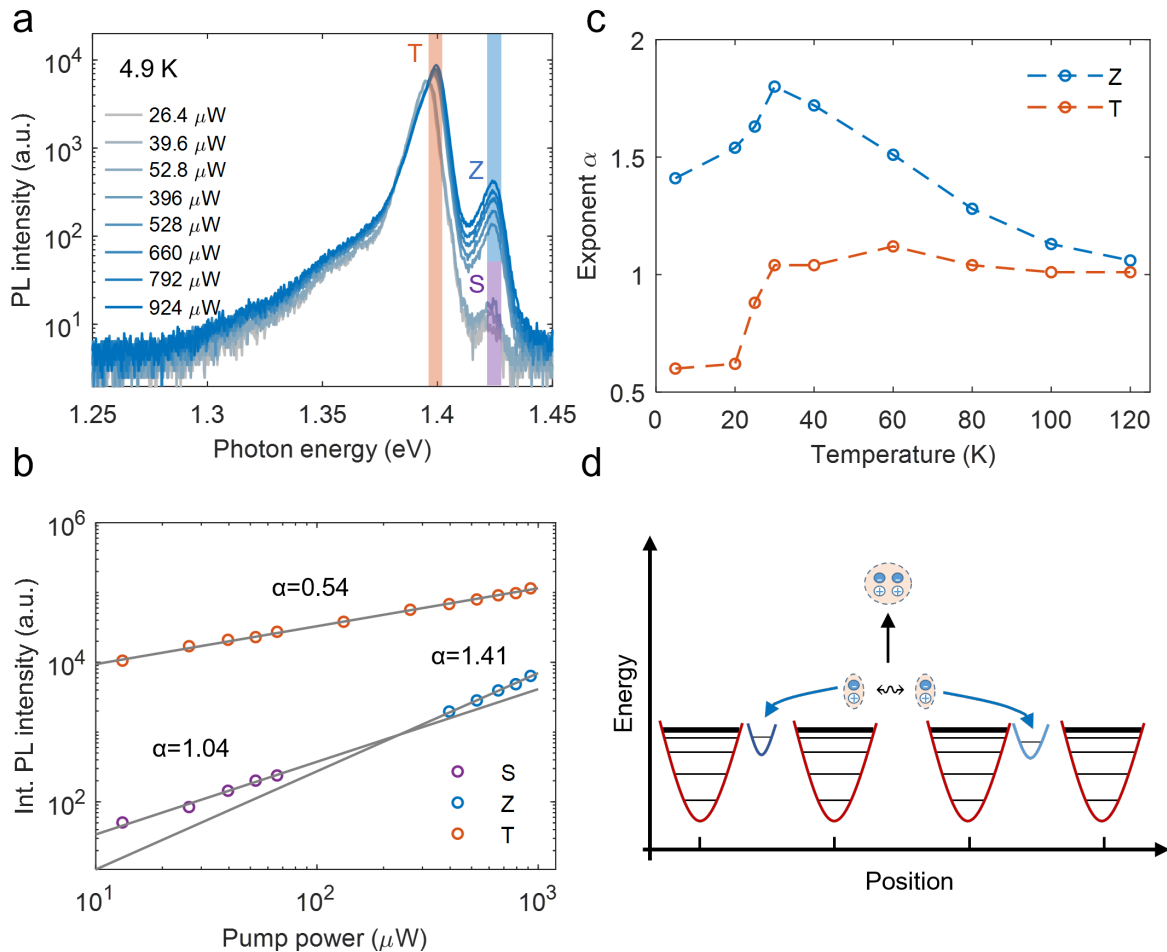


FIG. 4. Optical signatures of the emergence of biexcitons in the strong excitation regime. (a) PL spectrum in dependence of pump power at  $T = 4.9$  K. (b) Logarithmic plot of the S, Z, and T emission intensity as a function of pump power with an integrated spectral range of  $\sim 6$  meV marked in (a). (c) Temperature-dependent slope of the integrated Z and T emission. The dashed line is a guide to the eye. (d) Schematic illustration of the formation of the biexciton with the presence of the two types of potential traps. The blue arrows represent the formation of type-i IXs and the black arrow represents the formation of interlayer biexciton with repulsive exciton interaction.

ally filled. When further increasing the pump power, the occupation of IX in higher energy levels increases. However, the higher energy states in the moiré potential with their small energy spacing cannot confine IXs tightly. Instead, the IX will be trapped in the type-i defect-related potential. Then, type-i potentials can act as loss channels that reduce the IX density, where a large value is required to form IXX. Efficient quenching of the occupation of IXs in type-i potentials at a higher temperature of 30 K (see Fig. 2d) leads to the increase in the formation of IXX, and, thus, to the maximum value of  $\alpha$  for the Z peak. When further increasing the temperature, the value of  $\alpha$  of the Z peak monotonically decreases, possibly due to temperature-induced dissociation of IXXs, resulting in an increased occupation probability of the S-state (see Fig. S10).

#### IV. CONCLUSIONS

We have demonstrated the presence of two types of potential traps in the same twisted  $\text{MoSe}_2/\text{WSe}_2$  heterobilayer, denoted as type-i and type-ii, which we identified as traps related to optically active defect states and to the moiré potential, respectively. The type-i potential is shallow and dominates the PL emission of the heterobilayer under weak excitation at temperatures lower than 30 K. Starting at a temperature of about 30 K, the moiré-related multi-peaked emission feature known from TMD heterobilayers becomes clearly visible at higher excitation powers. Importantly, we observe the formation of interlayer biexcitons at even higher excitation power, whose formation peaks at a temperature of 30 K. We, thus, find that the shallow type-i potential acts as a loss channel for the formation of biexcitons.

Our work clearly identifies the different tempera-

ture and excitation regimes required to observe emissions related to localized excitons and biexcitons in a MoSe<sub>2</sub>/WSe<sub>2</sub> heterobilayer. Thus, our results lay the foundation for future detailed studies on the important formation dynamics of these types of excitons via ultrafast pump-probe measurements [6, 43]. Understanding the different competing traps in TMD heterobilayers, foremost moiré superlattices in competition with defect-related potential traps, and the regime required to generate biexcitons is key for the use of localized excitons and biexcitons in photonic quantum technologies [12], many-body physics [18], and nonlinear optics [17].

## ACKNOWLEDGMENTS

H. F. and W. W. acknowledge support by Olle Engkvists Stiftelse, Carl Tryggers Stiftelse, and together with S. D. by Chalmers Area of Advance Nano. W. W. acknowledges support by the Knut and Alice Wallenberg Foundation through a Wallenberg Academy Fellowship. Samples were fabricated in the Myfab Nanofabrication Laboratory at Chalmers. S. D. acknowledges financial support from European Union Graphene Flagship (Core 3, No. 881603), 2D TECH VINNOVA center (No. 2019-00068). Q. L. and S. X. acknowledge the support from the Independent Research Fund Denmark (project no. 9041-00333B and 2032-00351B), Direktør Ib Henriksens Fond, and Brødrene Hartmanns Fond. Y. Z. and Z. S. acknowledge the support from Horizon Europe (HORIZON) Project: ChirLog (101067269), the Academy of Finland (grants 314810, 333982, 336144, 336818, 352780, and 353364), Academy of Finland Flagship Programme (320167, PREIN), the EU H2020-MSCA-RISE-872049 (IPN-Bio), and ERC advanced grant (834742). E. M. acknowledges support from Deutsche Forschungsgemeinschaft (DFG) via CRC 1083 (project B09).

## SUPPLEMENTAL MATERIAL

### S1. METHODS

#### A. Sample fabrication

TMD monolayers were prepared by mechanical exfoliation from flux-grown bulk crystals (2D semiconductors) using Nitto tape and polydimethylsiloxane (PDMS). The layer thickness was determined by assessing the optical contrast of microscope images of the samples and by identifying characteristics in their PL emission. The heterobilayers were aligned by the straight edges of the TMD monolayers and stacked with the PDMS method [44]. The twist angles are determined by the straight edges of the monolayers and the H-type stacking is confirmed by polarization-resolved second harmonic generation (SHG) measurements (see Fig. S1). Thin-hBN flakes used for encapsulating the heterobilayer were prepared on SiO<sub>2</sub>/Si substrate. The TMD heterobilayer and the hBN flakes were finally picked up by polycarbonate (PC) film and then placed onto fused silica [45]. The remaining PC film was removed by 1165 remover.

#### B. Optical spectroscopy

The schematic of the measurement setup for PL measurements is shown in Fig. S11. Regarding PL measurements, a 1.7 eV CW laser diode (LP730-SF15, Thorlabs) was used to pump the samples placed in a closed-cycle cryostat (AttoDry 800, Attocube) and a low-temperature objective with a numerical aperture (NA) of 0.81 (LT-APO/NIR/0.81, Attocube) was used for both excitation and collection. The laser light was blocked through long-pass spectral filters, and the PL signals were sent to a grating spectrometer (SR500i, Andor) with a cooled silicon array camera (DU416A-LDC-DD, Andor). Hyperspectral imaging is performed by moving the sample position with a scanner (ANSxy100lr/LT, Attocube) while taking the PL spectrum with the spectrometer. The data of the right panel of Fig. 2a are acquired with a grating of 1200 grooves/mm, i.e., with a high spectral resolution of  $\sim 35 \mu\text{eV}$ . The remaining data in Fig. 2 are acquired with a grating of 600 grooves/mm (a resolution of  $\sim 280 \mu\text{eV}$ ), which is a good trade-off between spectral resolution and sensitivity. The data in Fig. 1, 3, and 4, are acquired with a grating of 150 grooves/mm (a resolution of  $\sim 800 \mu\text{eV}$ ). Polarization-resolved PL measurements are performed by using a quarter-wave plate (QWP) placed after a beamsplitter (BS). Linear polarized laser emission is converted into circularly polarized light through the QWP to excite the sample (see Fig. S11 for details).

Time-resolved PL measurements were performed using a time-correlated single-photon counting technique with a time tagger (quTAG, quTools). We excited samples

with a 1.759 eV pulsed laser (LDH-IB-705-B, PicoQuant) with a tunable repetition rate. The PL signals with energies lower than 1.71 eV were sent to a single-photon detector (SPCM-AQRH-15-FC, Excelitas).

Polarization-dependent SHG measurements were used to identify the type of stacking of our heterobilayers and were carried out with an excitation energy of 1.292 eV (repetition rate 2 kHz) from an amplified Ti:sapphire femtosecond laser system (Spectra-Physics Solstice Ace). The polarization orientation of the excitation beam was tailored by rotating an HWP. The laser light after the HWP was focused onto the sample by a 40x objective lens (NA=0.75, Nikon). The transmitted SHG signal was collected by another 40x objective lens (NA=0.5, Nikon), and passed through a linear polarizer. A 700-nm short-pass filter was placed after the polarizer to cut off the excitation beam. The final signal was detected by a photomultiplier tube (PMT) (Hamamatsu).

#### C. Estimation of the depth of potential traps

The temperature-dependent PL intensity change can be described by the Arrhenius equation  $I = I_0[1 + a \exp(-E_A/k_B T)]^{-1}$  [46], where  $E_A$  is the thermal activation energy and  $a$  is a coefficient that is related to the quantum yield of the host material [47]. Through fitting, we obtain an  $E_A$  of  $\sim 4 \text{ meV}$  for the shallow type-i potential traps and  $E_A$  of  $\sim 27 \text{ meV}$  for the type-ii moiré potential.



**S2. ADDITIONAL FIGURES**

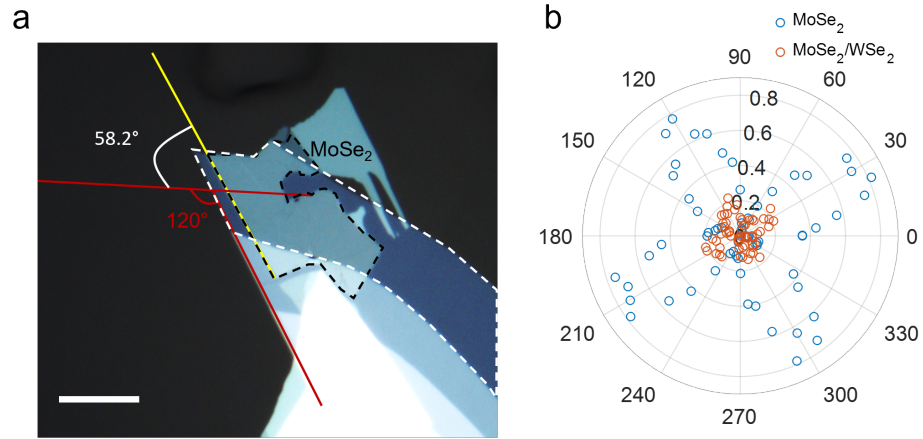


FIG. S1. Characterization of twist angle. (a) Optical image of the stacked MoSe<sub>2</sub>/WSe<sub>2</sub> heterobilayer on PDMS. The twist angle is measured 10 times according to the straight edges and determined to be  $58.2^\circ \pm 0.5^\circ$ . Scale bar:  $10 \mu\text{m}$ . (b) Polarization-resolved SHG measurement. The SHG intensity of the heterobilayer is remarkably weak compared to monolayer MoSe<sub>2</sub>, confirming that the stack type is H-stack [48].

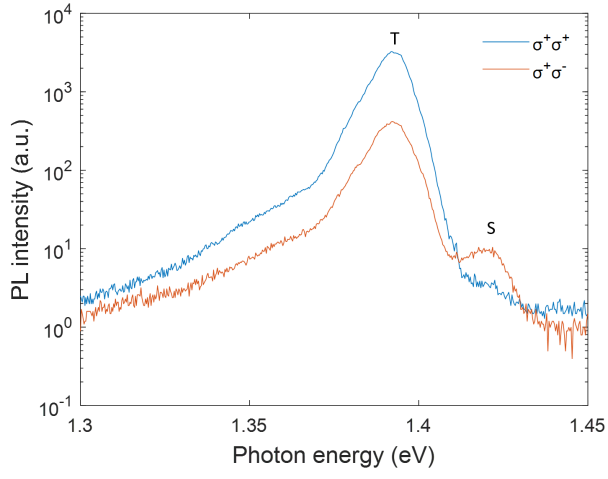


FIG. S2. Valley polarization of S and T with a pump power of  $66 \mu\text{W}$  at 4.9 K.

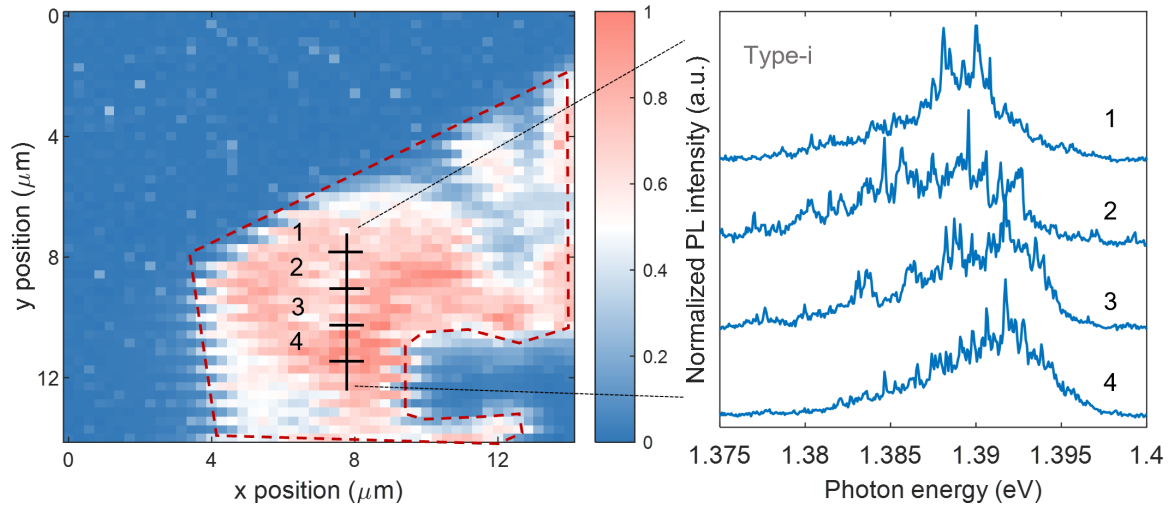


FIG. S3. Spatial distribution of type-i IXs. PL map obtained by integrating the PL spectrum between  $\sim 1.333$  and  $\sim 1.425$  eV at 4.9 K. The sharp emission lines (denoted as type-i) from the marked positions are shown in the right panel.



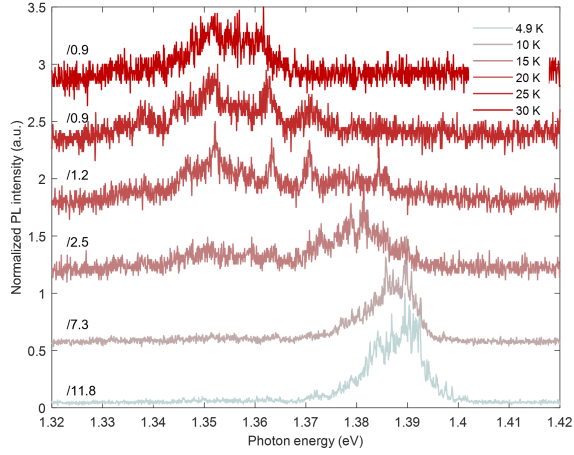


FIG. S4. PL emission as a function of temperature with a pump power of 33 nW. Each spectrum is normalized with its own peak intensity.

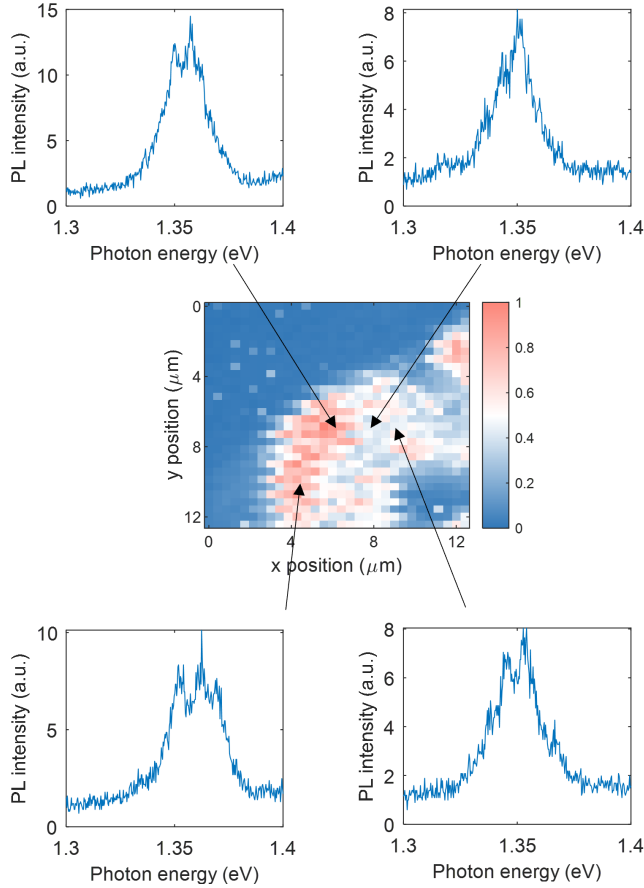


FIG. S5. PL map of type-ii localized IXs with a pump power of 330 nW at 40 K. The multipeak feature can be observed from various positions, however, the energy spacing between adjacent peaks varies with position. Such a variation will make it difficult to observe a twist angle-dependent energy spacing when comparing different samples.

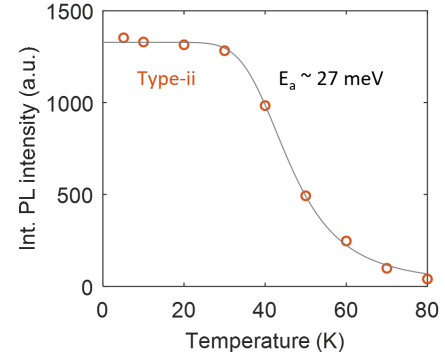


FIG. S6. Estimation of the depth of the type-ii potential via fitting by the Arrhenius equation. Note that the data is acquired from a different position than the inset shown in Fig. 2d of the main text.

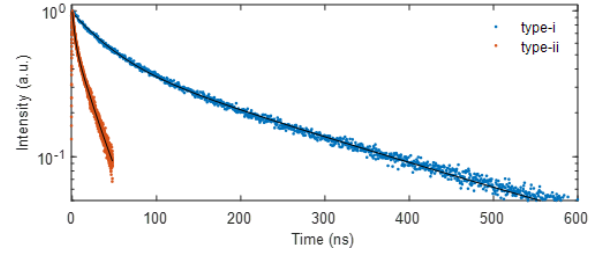


FIG. S7. Time-resolved PL dynamics of type-i and type-ii IXs. The solid lines represent the biexponential fits to the data, yielding the lifetime of type-i ( $\sim 40$  ns and  $\sim 235$  ns) and type-ii ( $\sim 3$  ns and  $\sim 23$  ns) IX. The lifetime of type-i (ii) localized IXs is measured at 4.9 K (40 K). Note that the measured type-i and type-ii IX lifetime is similar to the reported lifetime of sharp emission lines [23] and moiré-related peaks [14], respectively.

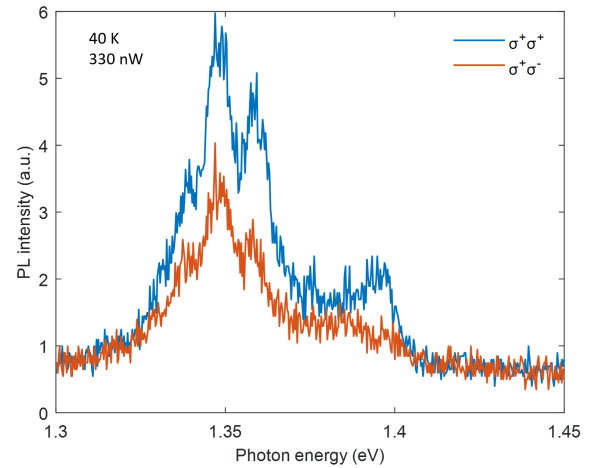


FIG. S8. Valley polarization of type-ii localized IXs with a pump power of 330 nW.

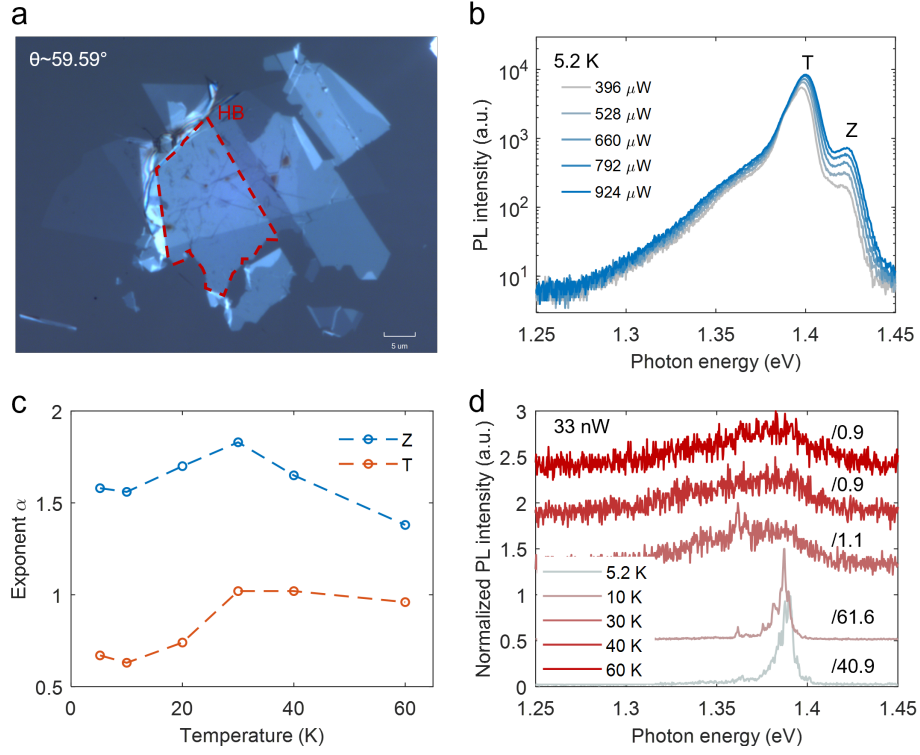


FIG. S9. Reproducibility of the temperature-dependent PL emission behavior in another sample. (a) optical image of the hBN-encapsulated  $\text{MoSe}_2/\text{WSe}_2$  heterobilayer. (b) Power-dependent PL spectrum in the high excitation regime. (c) Temperature-dependent change of exponent  $\alpha$ . (d) Evolution of PL spectrum with temperature. Each spectrum is normalized with its own peak intensity. No clear type-ii emissions emerge with increasing temperature, which is possibly due to the atomic reconstruction for the small twisted ( $< 1^\circ$ ) heterobilayer [28].

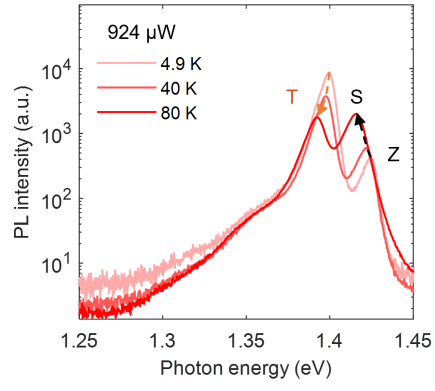


FIG. S10. Evolution of PL spectrum with a pump power of  $924 \mu\text{W}$ . With increasing temperature to 80 K, the IXX gradually vanishes (see Fig. 4c) and the S-IX takes over the emission peak. The increasing (decreasing) PL intensity of S(T)-IX with temperature is consistent with previous work [9].

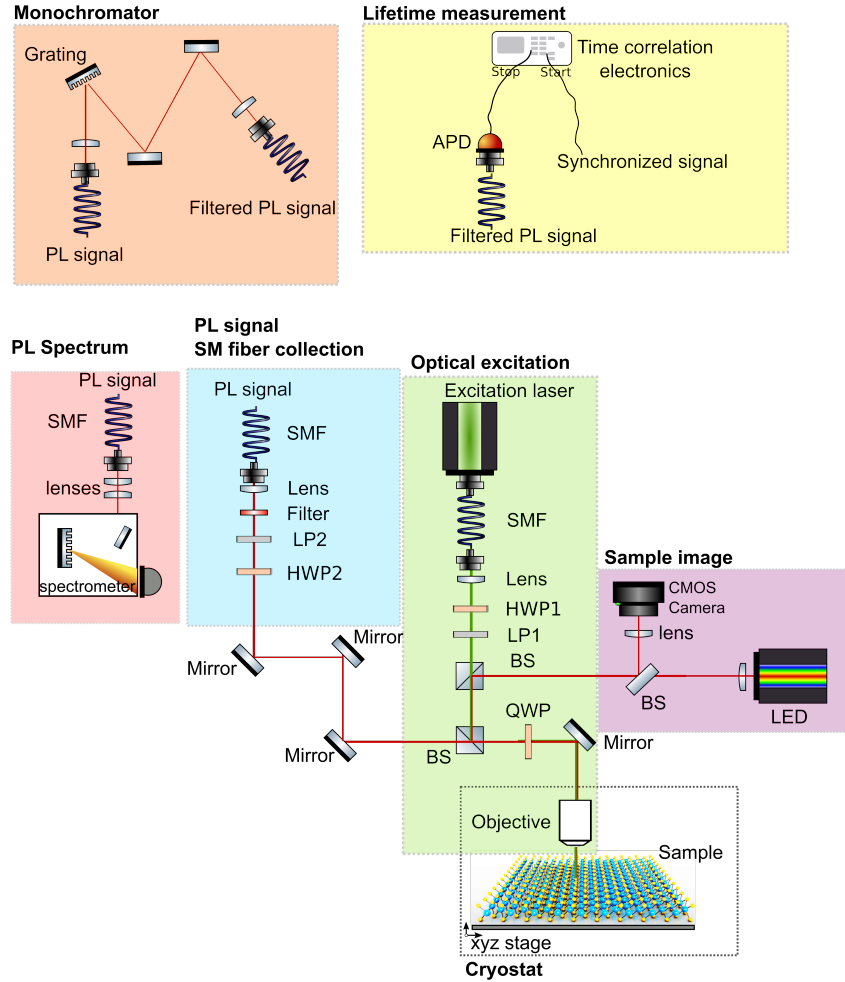


FIG. S11. Schematics of the PL measurement setup. LP: linear polarizer. HWP: half-waveplate. BS: beam splitter. SMF: single-mode fiber. The PL signal is sent to the spectrometer for measuring the PL spectrum, to the monochromator to filter the desired emission peak and measure exciton lifetime. LP1 is set to be horizontally linear polarized. LP2 and QWP are only used for valley polarization measurements. QWP is used to convert the linearly polarized laser emission to circularly polarized and then excite the sample. The circularly-polarized PL signal will be converted into a linear polarized signal, which is analyzed by LP through rotating HWP2. QWP and LP2 are removed when performing power- and temperature-dependent PL spectrum, and lifetime measurements.



- [1] N. P. Wilson, W. Yao, J. Shan, and X. Xu, Excitons and emergent quantum phenomena in stacked 2D semiconductors, *Nature* **599**, 383 (2021).
- [2] L. Du, M. R. Molas, Z. Huang, G. Zhang, F. Wang, and Z. Sun, Moiré photonics and optoelectronics, *Science* **379**, eadg0014 (2023).
- [3] E. M. Alexeev, D. A. Ruiz-Tijerina, M. Danovich, M. J. Hamer, D. J. Terry, P. K. Nayak, S. Ahn, S. Pak, J. Lee, J. I. Sohn, *et al.*, Resonantly hybridized excitons in moiré superlattices in van der Waals heterostructures, *Nature* **567**, 81 (2019).
- [4] J. Gu, L. Ma, S. Liu, K. Watanabe, T. Taniguchi, J. C. Hone, J. Shan, and K. F. Mak, Dipolar excitonic insulator in a moiré lattice, *Nature Physics* **18**, 395 (2022).
- [5] Z. Wang, D. A. Rhodes, K. Watanabe, T. Taniguchi, J. C. Hone, J. Shan, and K. F. Mak, Evidence of high-temperature exciton condensation in two-dimensional atomic double layers, *Nature* **574**, 76 (2019).
- [6] P. Merkl, F. Mooshammer, P. Steinleitner, A. Girnguber, K.-Q. Lin, P. Nagler, J. Holler, C. Schüller, J. M. Lupton, T. Korn, *et al.*, Ultrafast transition between exciton phases in van der waals heterostructures, *Nature materials* **18**, 691 (2019).
- [7] Y. Jiang, S. Chen, W. Zheng, B. Zheng, and A. Pan, Interlayer exciton formation, relaxation, and transport in TMD van der Waals heterostructures, *Light: Science & Applications* **10**, 72 (2021).
- [8] J. Choi, M. Florian, A. Steinhoff, D. Erben, K. Tran, D. S. Kim, L. Sun, J. Quan, R. Claassen, S. Majumder, *et al.*, Twist angle-dependent interlayer exciton lifetimes in van der waals heterostructures, *Physical Review Letters* **126**, 047401 (2021).
- [9] L. Zhang, R. Gogna, G. W. Burg, J. Horng, E. Paik, Y.-H. Chou, K. Kim, E. Tutuc, and H. Deng, Highly valley-polarized singlet and triplet interlayer excitons in van der Waals heterostructure, *Physical Review B* **100**, 041402 (2019).
- [10] F. Tagarelli, E. Lopriore, D. Erckensten, R. Perea-Causín, S. Brem, J. Hagel, Z. Sun, G. Pasquale, K. Watanabe, T. Taniguchi, *et al.*, Electrical control of hybrid exciton transport in a van der waals heterostructure, *Nature Photonics* **17**, 1 (2023).
- [11] A. Ciarrocchi, F. Tagarelli, A. Avsar, and A. Kis, Excitonic devices with van der Waals heterostructures: valleytronics meets twistrionics, *Nature Reviews Materials* **7**, 449 (2022).
- [12] H. Yu, G.-B. Liu, J. Tang, X. Xu, and W. Yao, Moiré excitons: From programmable quantum emitter arrays to spin-orbit-coupled artificial lattices, *Science Advances* **3**, e1701696 (2017).
- [13] S. Brem, C. Linderålv, P. Erhart, and E. Malic, Tunable phases of moiré excitons in van der Waals heterostructures, *Nano Letters* **20**, 8534 (2020).
- [14] K. Tran, G. Moody, F. Wu, X. Lu, J. Choi, K. Kim, A. Rai, D. A. Sanchez, J. Quan, A. Singh, *et al.*, Evidence for moiré excitons in van der Waals heterostructures, *Nature* **567**, 71 (2019).
- [15] E. Barré, O. Karni, E. Liu, A. L. O’Beirne, X. Chen, H. B. Ribeiro, L. Yu, B. Kim, K. Watanabe, T. Taniguchi, *et al.*, Optical absorption of interlayer excitons in transition-metal dichalcogenide heterostructures, *Science* **376**, 406 (2022).
- [16] Q. Lin, H. Fang, Y. Liu, Y. Zhang, M. Fischer, J. Li, J. Hagel, S. Brem, E. Malic, N. Stenger, *et al.*, A room-temperature moiré interlayer exciton laser, arXiv preprint arXiv:2302.01266 [10.48550/arXiv.2302.01266](https://doi.org/10.48550/arXiv.2302.01266) (2023).
- [17] A. Camacho-Guardian and N. R. Cooper, Moiré-induced optical nonlinearities: single-and multiphoton resonances, *Physical Review Letters* **128**, 207401 (2022).
- [18] A. Julku, Nonlocal interactions and supersolidity of moiré excitons, *Physical Review B* **106**, 035406 (2022).
- [19] O. Karni, E. Barré, V. Pareek, J. D. Georganas, M. K. Man, C. Sahoo, D. R. Bacon, X. Zhu, H. B. Ribeiro, A. L. O’Beirne, *et al.*, Structure of the moiré exciton captured by imaging its electron and hole, *Nature* **603**, 247 (2022).
- [20] D. Schmitt, J. P. Bange, W. Bennecke, A. AlMutairi, G. Meneghini, K. Watanabe, T. Taniguchi, D. Steil, D. R. Luke, R. T. Weitz, *et al.*, Formation of moiré interlayer excitons in space and time, *Nature* **608**, 499 (2022).
- [21] Z. Li, X. Lu, D. F. Cordovilla Leon, Z. Lyu, H. Xie, J. Hou, Y. Lu, X. Guo, A. Kaczmarek, T. Taniguchi, *et al.*, Interlayer exciton transport in MoSe<sub>2</sub>/WSe<sub>2</sub> heterostructures, *ACS nano* **15**, 1539 (2021).
- [22] S. Susarla, M. H. Naik, D. D. Blach, J. Zipfel, T. Taniguchi, K. Watanabe, L. Huang, R. Ramesh, F. H. da Jornada, S. G. Louie, *et al.*, Hyperspectral imaging of exciton confinement within a moiré unit cell with a subnanometer electron probe, *Science* **378**, 1235 (2022).
- [23] K. L. Seyler, P. Rivera, H. Yu, N. P. Wilson, E. L. Ray, D. G. Mandrus, J. Yan, W. Yao, and X. Xu, Signatures of moiré-trapped valley excitons in MoSe<sub>2</sub>/WSe<sub>2</sub> heterobilayers, *Nature* **567**, 66 (2019).
- [24] H. Baek, M. Brotons-Gisbert, Z. X. Koong, A. Campbell, M. Rambach, K. Watanabe, T. Taniguchi, and B. D. Gerardot, Highly energy-tunable quantum light from moiré-trapped excitons, *Science Advances* **6**, eaba8526 (2020).
- [25] H. Cai, A. Rasmita, Q. Tan, J.-M. Lai, R. He, D. Chen, N. Wang, Z. Mu, Z. Huang, Z. Zhang, *et al.*, Interlayer donor-acceptor pair excitons in MoSe<sub>2</sub>/WSe<sub>2</sub> moiré heterobilayer, arXiv preprint arXiv:2302.13003 [10.48550/arXiv.2302.13003](https://doi.org/10.48550/arXiv.2302.13003) (2023).
- [26] H. Zheng, B. Wu, S. Li, J. Ding, J. He, Z. Liu, C.-T. Wang, J.-T. Wang, A. Pan, and Y. Liu, Localization-enhanced moiré exciton in twisted transition metal dichalcogenide heterotrilinear superlattices, *Light: Science & Applications* **12**, 117 (2023).
- [27] A. Raja, L. Waldecker, J. Zipfel, Y. Cho, S. Brem, J. D. Ziegler, M. Kulig, T. Taniguchi, K. Watanabe, E. Malic, *et al.*, Dielectric disorder in two-dimensional materials, *Nature nanotechnology* **14**, 832 (2019).
- [28] M. R. Rosenberger, H.-J. Chuang, M. Phillips, V. P. Oleshko, K. M. McCreary, S. V. Sivaram, C. S. Hellberg, and B. T. Jonker, Twist angle-dependent atomic reconstruction and moiré patterns in transition metal dichalcogenide heterostructures, *ACS nano* **14**, 4550 (2020).
- [29] H. Yu, G.-B. Liu, and W. Yao, Brightened spin-triplet interlayer excitons and optical selection rules in van der Waals heterobilayers, *2D Materials* **5**, 035021 (2018).
- [30] T. Wang, S. Miao, Z. Li, Y. Meng, Z. Lu, Z. Lian, M. Blei, T. Taniguchi, K. Watanabe, S. Tongay, *et al.*, Giant valley-zeeman splitting from spin-singlet and spin-

- triplet interlayer excitons in WSe<sub>2</sub>/MoSe<sub>2</sub> heterostructure, *Nano Letters* **20**, 694 (2019).
- [31] H. Kim, K. Aino, K. Shinokita, W. Zhang, K. Watanabe, T. Taniguchi, and K. Matsuda, Dynamics of moiré exciton in a twisted MoSe<sub>2</sub>/WSe<sub>2</sub> heterobilayer, *Advanced Optical Materials*, 2300146 (2023).
- [32] F. Mahdikhanyarvejahany, D. N. Shanks, M. Klein, Q. Wang, M. R. Koehler, D. G. Mandrus, T. Taniguchi, K. Watanabe, O. L. Monti, B. J. LeRoy, *et al.*, Localized interlayer excitons in MoSe<sub>2</sub>-WSe<sub>2</sub> heterostructures without a moiré potential, *Nature Communications* **13**, 5354 (2022).
- [33] Q. Tan, A. Rasmita, Z. Zhang, K. Novoselov, and W.-b. Gao, Signature of cascade transitions between interlayer excitons in a moiré superlattice, *Physical Review Letters* **129**, 247401 (2022).
- [34] H. Guo, X. Zhang, and G. Lu, Moiré excitons in defective van der Waals heterostructures, *Proceedings of the National Academy of Sciences* **118**, e2105468118 (2021).
- [35] Y.-M. He, G. Clark, J. R. Schaibley, Y. He, M.-C. Chen, Y.-J. Wei, X. Ding, Q. Zhang, W. Yao, X. Xu, *et al.*, Single quantum emitters in monolayer semiconductors, *Nature nanotechnology* **10**, 497 (2015).
- [36] Y.-M. He, S. Höfling, and C. Schneider, Phonon induced line broadening and population of the dark exciton in a deeply trapped localized emitter in monolayer WSe<sub>2</sub>, *Optics express* **24**, 8066 (2016).
- [37] D. Edelberg, D. Rhodes, A. Kerelsky, B. Kim, J. Wang, A. Zangiabadi, C. Kim, A. Abhinandan, J. Ardelean, M. Scully, *et al.*, Approaching the intrinsic limit in transition metal diselenides via point defect control, *Nano letters* **19**, 4371 (2019).
- [38] Y. You, X.-X. Zhang, T. C. Berkelbach, M. S. Hybertsen, D. R. Reichman, and T. F. Heinz, Observation of biexcitons in monolayer WSe<sub>2</sub>, *Nature Physics* **11**, 477 (2015).
- [39] R. Phillips, D. Loring, G. Denton, and G. Smith, Biexciton creation and recombination in a GaAs quantum well, *Physical Review B* **45**, 4308 (1992).
- [40] G. Haider, K. Sampathkumar, T. Verhagen, L. Nádvořník, F. J. Sonia, V. Valeš, J. Šykora, P. Kapusta, P. Němec, M. Hof, *et al.*, Superradiant emission from coherent excitons in van der Waals heterostructures, *Advanced Functional Materials* **31**, 2102196 (2021).
- [41] V. I. Klimov, S. A. Ivanov, J. Nanda, M. Achermann, I. Bezel, J. A. McGuire, and A. Piryatinski, Single-exciton optical gain in semiconductor nanocrystals, *Nature* **447**, 441 (2007).
- [42] W. Li, X. Lu, S. Dubey, L. Devenica, and A. Srivastava, Dipolar interactions between localized interlayer excitons in van der Waals heterostructures, *Nature Materials* **19**, 624 (2020).
- [43] L. Yuan, B. Zheng, J. Kunstmann, T. Brumme, A. B. Kuc, C. Ma, S. Deng, D. Blach, A. Pan, and L. Huang, Twist-angle-dependent interlayer exciton diffusion in WS<sub>2</sub>-WSe<sub>2</sub> heterobilayers, *Nature materials* **19**, 617 (2020).
- [44] A. Castellanos-Gomez, M. Buscema, R. Molenaar, V. Singh, L. Janssen, H. S. Van Der Zant, and G. A. Steele, Deterministic transfer of two-dimensional materials by all-dry viscoelastic stamping, *2D Materials* **1**, 011002 (2014).
- [45] P. Zomer, M. Guimarães, J. Brant, N. Tombros, and B. Van Wees, Fast pick up technique for high quality heterostructures of bilayer graphene and hexagonal boron nitride, *Applied Physics Letters* **105**, 013101 (2014).
- [46] Y. Luo, N. Liu, X. Li, J. C. Hone, and S. Strauf, Single photon emission in WSe<sub>2</sub> up to 160 K by quantum yield control, *2D Materials* **6**, 035017 (2019).
- [47] M. Leroux, N. Grandjean, B. Beaumont, G. Nataf, F. Semond, J. Massies, and P. Gibart, Temperature quenching of photoluminescence intensities in undoped and doped GaN, *Journal of Applied Physics* **86**, 3721 (1999).
- [48] W.-T. Hsu, Z.-A. Zhao, L.-J. Li, C.-H. Chen, M.-H. Chiu, P.-S. Chang, Y.-C. Chou, and W.-H. Chang, Second harmonic generation from artificially stacked transition metal dichalcogenide twisted bilayers, *ACS nano* **8**, 2951 (2014).